Article

Application and Optimization of a Fast Non-Local Means Noise Reduction Algorithm in Pediatric Abdominal Virtual Monoenergetic Images

Hajin Kim [1], Juho Park [2], Jina Shim [3] and Youngjin Lee [2,*]

[1] Department of Health Science, General Graduate School, Gachon University, 191, Hambakmoe-ro, Yeonsu-gu, Incheon 21936, Republic of Korea; happida3@gachon.ac.kr
[2] Department of Radiological Science, Gachon University, 191, Hambakmoe-ro, Yeonsu-gu, Incheon 21936, Republic of Korea; qnlals123@gachon.ac.kr
[3] Department of Diagnostic Radiology, Severance Hospital, 50-1, Yonsei-ro, Seodaemun-gu, Seoul 03722, Republic of Korea; eoeornfl@yuhs.ac
[*] Correspondence: yj20@gachon.ac.kr; Tel.: +82-32-820-4362

Abstract: In this study, we applied and optimized a fast non-local means (FNLM) algorithm to reduce noise in pediatric abdominal virtual monoenergetic images (VMIs). To analyze various contrast agent concentrations, we produced contrast agent concentration samples (20, 40, 60, 80, and 100%) and inserted them into a phantom model of a one-year-old pediatric patient. Single-energy computed tomography (SECT) and dual-energy computed tomography (DECT) images were acquired from the phantom, and 40 kilo-electron-volt (keV) VMI was acquired based on the DECT images. For the 40 keV VMI, the smoothing factor of the FNLM algorithm was applied from 0.01 to 1.00 in increments of 0.01. We derived the optimized value of the FNLM algorithm based on quantitative evaluation and performed a comparative assessment with SECT, DECT, and a total variation (TV) algorithm. As a result of the analysis, we found that the average contrast to noise ratio (CNR) and coefficient of variation (COV) of each concentration were most improved at a smoothing factor of 0.02. Based on these results, we derived the optimized smoothing factor value of 0.02. Comparative evaluation shows that the optimized FNLM algorithm improves the CNR and COV results by approximately 3.14 and 2.45 times, respectively, compared with the DECT image, and the normalized noise power spectrum result shows a 10^{-1} mm^2 improvement. The main contribution of this study is to demonstrate the effectiveness of an optimized FNLM algorithm in reducing noise in pediatric abdominal VMI, allowing high-quality images to be acquired while reducing contrast dose. This advancement has significant implications for minimizing the risk of contrast-induced toxicity, especially in pediatric patients. Our approach addresses the problem of limited datasets in pediatric imaging by providing a computationally efficient noise reduction technique and highlights the clinical applicability of the FNLM algorithm. In addition, effective noise reduction enables high-contrast imaging with minimal radiation and contrast exposure, which is expected to be suitable for repeat CT examinations of pediatric liver cancer patients and other abdominal diseases.

Keywords: fast non-local means algorithm; virtual monoenergetic image; optimize the smoothing factor; quantitative evaluation of image quality; pediatric abdominal computed tomography image

1. Introduction

In recent years, computed tomography (CT) has become widely used in clinical practice because of its ability to provide high-quality three-dimensional (3D) image acquisition within a short acquisition time, low cost to the patient, and high diagnostic accuracy for abdominal examinations [1]. According to a 2024 report by the Organization for Economic Co-operation and Development (OECD), in 2021, more than 80 million CT examinations

were performed annually in the United States, while in South Korea, CT examinations accounted for the highest number of medical diagnostic devices used [2].

Abdominal CT is commonly employed for the anatomical evaluation of the surgical area and to assess treatment effectiveness in pediatric liver cancer patients. However, pediatric patients are more sensitive to radiation due to their immature cells; thus, high radiation doses can potentially cause side- or long-term effects. Furthermore, pediatric patients have thinner body walls, which reduces the radiation filtering effect and increases radiation exposure to deeply located organs, thus requiring special consideration [3]. These concerns regarding radiation exposure have led to recommendations for replacing liver examinations in pediatric patients with ultrasound and magnetic resonance imaging (MRI) scans. However, CT scans are essential for evaluating pediatric liver cancer patients undergoing liver transplantation [4,5].

To reduce radiation exposure in pediatric liver examinations, CT scans of pediatric patients with liver cancer have been conducted using lower tube voltages and currents than adult protocols, focusing primarily on end-artery and hepatic vein assessment [6]. However, reducing the radiation dose can lead to lower image contrast and diminished diagnostic accuracy. Additionally, liver CT examinations require higher contrast agent doses to enhance blood vessel visibility, which aids in diagnosis by improving the detection of microvessels. However, the use of contrast agents can cause nephrotoxicity, particularly in pediatric patients, as repeated use increases the risk of kidney dysfunction [7]. This limitation of contrast agents can reduce image contrast and complicate vascular assessments, especially in pediatric liver transplant cases that require high contrast enhancement [8].

To address these challenges, photon-counting detectors (PCDs) have been introduced as hardware solutions [9,10]. By allowing the selection of specific energy ranges, PCD technology enhances image contrast for targeted tissues or materials. Furthermore, images acquired using low-energy photons improve contrast while reducing the radiation dose, resulting in images with higher diagnostic value. However, the commercialization of PCDs remains limited due to various factors, such as size and cost [11].

The virtual monoenergetic image (VMI) approach based on dual-energy CT (DECT) is a software-based technique used to address the limitations of hardware-based PCD. DECT acquires images in low- and high-energy data and uses the attenuation differences of X-rays at different energies to distinguish between materials [12]. Based on this characteristic, a VMI generated from a DECT-acquired image at various energy levels can select a specific energy range to increase contrast in vascularized areas, thereby improving the diagnostic accuracy of lesions. In particular, for liver CT examinations, iodine is widely used as a contrast agent, and a VMI with a low single-energy level (i.e., 40–50 kilo-electron-volt (keV)) is close to the K-edge of iodine (33.2 keV), which is beneficial for observing liver lesions, thus increasing the diagnosis rate [13,14].

Preliminary studies have shown that a 40 keV VMI acquired with DECT provides images with higher Hounsfield unit (HU) values than single-energy CT (SECT) images at the same contrast concentration, achieving a 20% reduction in contrast concentration [15]. Additionally, one study found that VMI imaging at 40 keV improved diagnostic reliability and increased laceration clarity when evaluating pancreatic imaging [16]. When compared with SECT, the 40 keV VMI has higher HU values in the contrast region; however, image quality is degraded by statistical noise caused by an insufficient number of photons at lower energy levels [17,18]. In one study, the CNR values of a 40 keV VMI and single-energy CT were measured and found to be about 3.68 and 4.27, respectively, indicating a decrease in image quality in VMI images acquired in the low energy range [19]. Therefore, effective noise reduction by applying a denoising algorithm to 40 keV VMI acquired by DECT can reduce the contrast agent dose and concentration, as well as the radiation dose to the patient.

To reduce noise in CT images, algorithms, such as median, Gaussian, and Wiener filters, have been proposed and proven useful [20,21]. However, conventional noise reduction algorithms decrease the sharpness of image edges and cause a blurring effect, reducing

resolution. To address these issues, non-local means (NLM) algorithms have been proposed to reduce noise by using the intensity and relative distance of pixels in the image to preserve the sharpness of the edge; however, conventional NLM algorithms are computationally intensive, resulting in difficulties in clinical applications where fast image acquisition is essential [22]. To solve this problem, the proposed fast NLM (FNLM) algorithm simplifies processing by converting the process of calculating weights from two dimensions to one, shortening the computation time, and its usefulness has been proven [23,24]. Many studies have been conducted on image quality evaluation and noise reduction in VMIs; however, most of these studies have focused on adults, and relatively few studies have performed quantitative evaluation by comparing them with existing algorithms.

Therefore, the purpose of this study was to apply the FNLM algorithm to pediatric abdominal 40 keV VMIs acquired by DECT to derive optimization values and to quantitatively evaluate the usefulness of the FNLM algorithm by comparative evaluation with conventional algorithms.

The remainder of this paper is organized as follows: Section 2 describes the materials and methods of the study, including the contrast sample preparation and phantom setup, image acquisition parameters, modeling of the fast non-local means noise reduction algorithm, and image quality evaluation. Section 3 describes the optimization of the fast non-local means noise reduction algorithm, its comparative evaluation with conventional algorithms, and a visual evaluation. Section 4 discusses the significance of our results, and Section 5 summarizes the contributions and future research directions of our study.

2. Materials and Methods

2.1. Preparation of Contrast Agent Samples and Pediatric Abdominal Phantom Setup

In this study, a one-year-old pediatric phantom (Model No. 704), ATOM (CIRS, Norfolk, VA, USA), was used to simulate a pediatric patient. To prepare five contrast agent concentration samples, saline was diluted to a contrast agent concentration of 300 mg/mL. A reference sample with an iodine concentration of 11.5 mg/mL and an average Hounsfield unit (HU) value of 341 was set to a 100% concentration. Four additional samples were prepared by decreasing the concentration at 20% intervals and then placed in polypropylene microtubes (14 mm diameter, 40 mm length) to prepare 20, 40, 60, and 80% contrast agent samples. The phantom weighed less than 15 kg, and the prepared contrast agent samples were inserted into the upper abdomen of the pediatric phantom. Figure 1 shows the phantom used in the experiment.
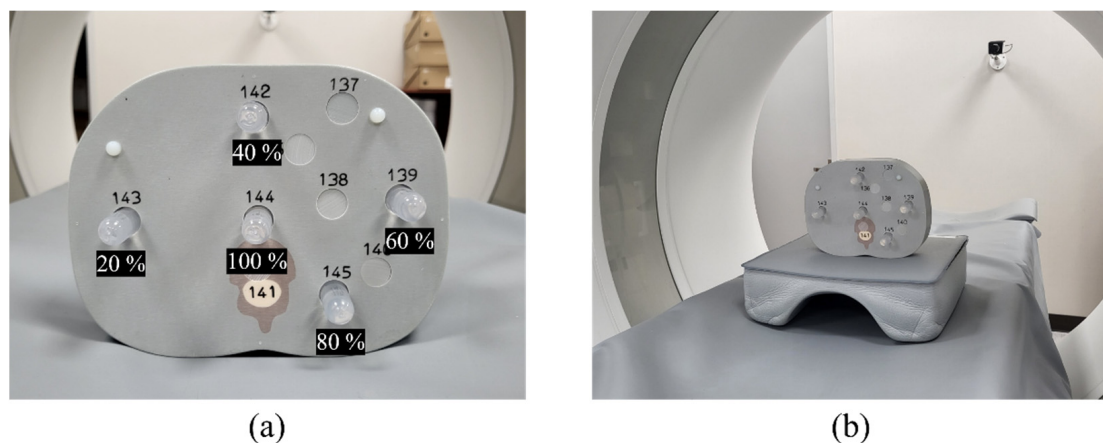

(a)   (b)

Figure 1. ATOM phantom images for CT image acquisition: (**a**) ATOM phantom with iodine contrast agents of various concentrations (100, 80, 60, 40, and 20%) and (**b**) set up phantom positions.

2.2. The Acquisition Parameters of Computed Tomography Images

For image acquisition, we used a Somatom Definition Force (Siemens Healthcare, Forchheim, Germany) and a picture archiving and communication system (GE Centricity

RA 1000, GE Healthcare, Chicago, IL, USA). The syngo.via VB40A software (Siemens Healthcare, Forchheim, Germany) was used to obtain the reconstructed VMI. The CT scan parameters are presented in Table 1. To perform both SECT and DECT scans, the CT dose index volume was set to 0.8 mGy. For the SECT scan, the tube voltage was set to 70 kV; for the DECT scan, images were acquired with the high tube voltage fixed at 150 kV, and the low tube voltage was increased in 10 kV increments from 70 kV to 100 kV.

Table 1. Acquisition parameters of computed tomography (CT) for single-energy CT (SECT) and dual-energy CT (DECT) images.

Scan Parameter				Value
CTDIvol (mGy)				0.8
Pitch				1
Rotation time (sec)				0.25
Reconstruction method				ADMIRE (strength 3 + Br40)
Slice thickness/increment (mm)				3/3
Scanmethod	SECT		kV	70
			mAs	89
	DECT	kV	A tube	70, 80, 90, 100
			B tube	150 (Sn filter)
		mAs	A tube	40, 22, 16, 14
			B tube	10, 11, 10, 7

2.3. Fast Non-Local Means Noise Reduction Algorithm Modeling

The NLM noise reduction algorithm has demonstrated significant effectiveness for noise reduction [25]. Moreover, the NLM effectively addresses issues commonly encountered with local filtering techniques, such as signal distortion and blurring. This is because the NLM noise reduction algorithm compares the overall geometric composition using the Euclidean distance as a weight, rather than applying a sliding technique to the entire image, as in the Gaussian and Wiener filters. The NLM noise reduction algorithm is defined as follows:

$$g'_{NLM}(i) = \frac{1}{Z(i)} \sum_{i \in N(i)} \omega(i,j) f(x)(j) \tag{1}$$

where $f(x)$ represents original noisy image and i represents an arbitrary point in the image (g'_{NLM}) restored by NLM. $Z(i)$ denotes the normalization coefficient, $N(i)$ denotes the search window, which indicates the normalization constant corresponding to the region adjacent to i, and $\omega(i,j)$ denotes the distance weight according to the similarity between the square kernels centered on arbitrary point i and j.

The l_2-norm (Euclidean distance) is used to calculate the distance weight between the kernels. The Euclidean distance between the two kernels is calculated as follows:

$$Euclidean\ distance = \|k_i - k_j\|_2^2 \tag{2}$$

where k_i represents the kernel included in the pixel to be filtered and k_j represents another kernel within the search window.

Based on the Euclidean distance, the weight $\omega(i,j)$ is calculated as follows:

$$\omega(i,j) = \frac{1}{Z(i)} exp\left(-\frac{G_n(\delta)\|k_i - k_j\|_{2,a}^2}{h^2}\right) \tag{3}$$

where G_n denotes a Gaussian distribution with a standard deviation of magnitude a, δ denotes the adjacent area, and h denotes a constant smoothing factor. Each weight ω must

be within the range of $0 \leq \omega \leq 1$, and the sum of the weights for each kernel must be 1. Therefore, $Z(i)$ is defined according to Equation (4), as follows:

$$Z(i) = \sum_i exp\left(-\frac{G_n(\delta)\|k_i - k_j\|_{2,a}^2}{h^2}\right) \tag{4}$$

The FNLM noise reduction algorithm modifies the calculation of $\omega(i,j)$ in the NLM noise reduction algorithm from two dimensions (2D) to one dimension (1D). The modified $\omega(m,n)$ is defined as follows:

$$\omega(i,j) = \frac{1}{Z(i)}S(f(x)(i+P) - f(x)(i-P)) \tag{5}$$

where P denotes the size of the local kernel when vectorization is performed from 2D to 1D, and S can be obtained using Equation (6), as follows:

$$S(p) = \sum_{n=0}^{p} exp\left(-\frac{\|f(x)(n) - f(x)(n+\gamma)\|_2^2}{h^2}\right) \tag{6}$$

where γ denotes $j - i$, and p denotes $I + \gamma$.

The FNLM noise reduction algorithm improves the time resolution compared to the NLM noise reduction algorithm [24]. This enhancement was achieved by simplifying the process by using one-dimensional computations.

2.4. Image Quality Evaluations

In our study, VMI was compared and evaluated using 40 keV imaging, an energy level that has been empirically validated as effective in abdominal diagnosis. This energy level was selected because of its proven ability to provide superior contrast enhancement, substantiating the superiority observed in our previous study. To optimize the smoothing factor of the FNLM noise reduction algorithm, we enlarged the region of interest (ROI) at the center of the five contrast agent concentration samples and averaged the results. For a quantitative evaluation of the optimized FNLM, we used MATLAB software (ver. 2023a; MathWorks, Boston, MA, USA) to calculate the contrast to noise ratio (CNR) and coefficient of variation (COV) [26,27]. Figure 2 shows the ROI: the yellow and red boxes indicate the materials and background regions for the noise level evaluation, the blue box represents the region for the visual evaluation, and the white box indicates the region for the normalized noise power spectrum (NNPS) evaluation.
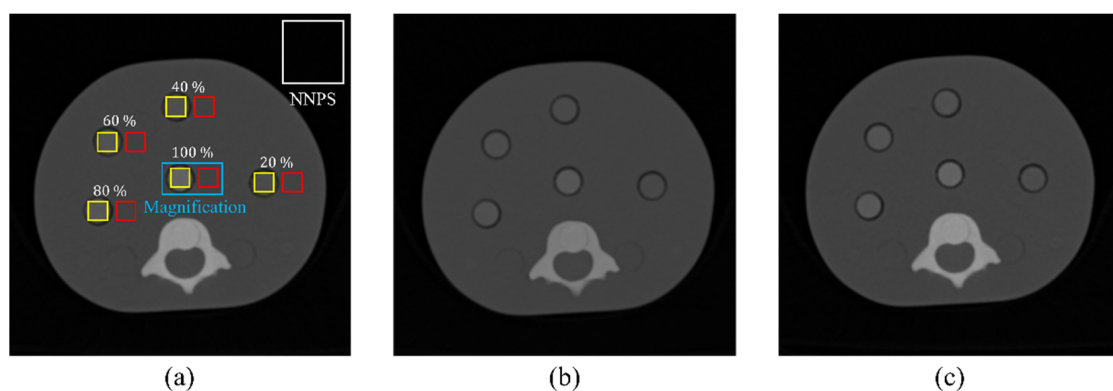

(a)   (b)   (c)

Figure 2. Computed tomography scans acquired ATOM phantom images: (**a**) region of interest for quantitative and visual evaluation, (**b**) single-energy computed tomography image, and (**c**) dual -energy computed tomography image.

The CNR indicates the ratio of contrast and noise between the ROI and the background region of the same image. Equation (7) is as follows:

$$CNR = \frac{|S_R - S_{BK}|}{\sqrt{\sigma_R^2 + \sigma_{BK}^2}} \tag{7}$$

where S_R and S_{BK} represent the average signal intensities in the ROI and background, respectively; σ_R and σ_{BK} are standard deviations in the ROI and background, respectively. The COV was calculated to assess the degree of deviation in the phantom images, as in Equation (8):

$$COV = \frac{\sigma_R}{\mu} \tag{8}$$

where σ_R is the standard deviation of the signal intensity and μ is the average value in the ROI.

Moreover, for comparative evaluation, the optimized FNLM was compared with SECT, DECT, and total variation (TV) algorithm images. The TV algorithm can effectively reduce noise without losing high-frequency signals. The algorithm determines specific settings for a particular region based on the pixel values in the ROI and reflects the interrelationships between composition changes across the overall image [28]. The TV algorithm formula is as follows:

$$g(x,y) = f(x,y) + n(x,y) \tag{9}$$

where $f(x,y)$ represents the ideal image, $n(x,y)$ represents the electrical noise introduced during image acquisition, and $g(x,y)$ signifies the resulting degraded image.

In addition, the gradient used to calculate the difference between the pixel value in the ROI and its neighboring pixels is defined as follows:

$$
\begin{aligned}
f(m,n)_{TV} &= \sum_{m=1}^{M}\sum_{n=1}^{N}|\nabla f(m,n)| \\
&= \sum_{m=1}^{M}\sum_{n=1}^{N}\sqrt{(f(m,n)-f(m-1,n))^2 + (f(m,n)-f(m,n-1))^2}
\end{aligned} \tag{10}
$$

where $f(x,y)$ represents the image function, with M and N indicating the number of rows and columns of the image $f(m,n)$, respectively, while ∇ denotes the gradient operator.

In general, the l_2-norm is considered to be an effective operator for extracting edges. However, the l_2-norm is highly sensitive to noise, which means that it has a high risk of incorrect signal processing in that it selects noisy signals over edge signals. Therefore, we used the l_1-norm as the gradient operator. Based on Equation (10), we designed a TV denoising algorithm, which is represented by the following Equation (11):

$$\varnothing(f(m,n)|I(m,n)) = \sum_{m=1}^{M}\sum_{n=1}^{N}|\nabla f(m,n)| + \frac{\gamma}{2}I(m,n) - f(m,n)_2 \tag{11}$$

where γ represents a control parameter with two terms on the righthand side of the equation, and in our study, we set $\gamma = 0.1$. Moreover, $\sum_{m=1}^{M}\sum_{n=1}^{N}|\nabla f(m,n)|$ can be used to determine the optimal solution. $\frac{\gamma}{2}I(m,n) - f(m,n)_2$ represents the regulation fidelity term that indicates the accuracy of the image information.

Lastly, we used an adaptive average filter method, which applies the weighted value of the ROI and neighborhood pixel value through iterative utilization of Equation (11).

To quantitatively evaluate image quality, we calculated the CNR, COV, and NNPS. The NNPS parameter analyzes the noise variations in an image across the spatial frequency range of interest [29]. The NNPS calculations were based on measurements in air. The equation for calculating NNPS is as follows:

$$NNPS_{normalized}(u,v) = \frac{NPS(u,v)}{(large\ area\ signal)^2} \tag{12}$$

where *u* and *v* denote the pixel signal along the *X*- and *Y*-axes, respectively.

3. Results

3.1. The Optimization of the Fast Non-Local Means Noise Reduction Algorithm

A quantitative evaluation was conducted to determine the optimized smoothing factor for the FNLM noise reduction algorithm. The CNR and COV were calculated as evaluation factors to optimize the smoothing factor for the FNLM. Figure 3 shows the graph of the average CNR and COV at each contrast concentration with increasing smoothing factors. The CNR evaluation showed the highest value (40.2996) at a smoothing factor of 0.02 across all contrast concentrations and then rapidly decreased with a steep slope, eventually converging to a constant value. The COV evaluation showed the lowest value of 0.0055 at a smoothing factor of 0.02 for all contrast concentrations and then increased significantly from 0.02, eventually converging to a constant value. When analyzing the CNR and COV, the FNLM algorithm achieved the lowest COV at a smoothing factor of 0.02, minimizing noise variability while providing the highest value of CNR, resulting in improved image contrast. Therefore, based on these results, we derived a smoothing factor of 0.02 as the optimal value, which achieves the highest CNR and lowest COV simultaneously to determine the optimized value.
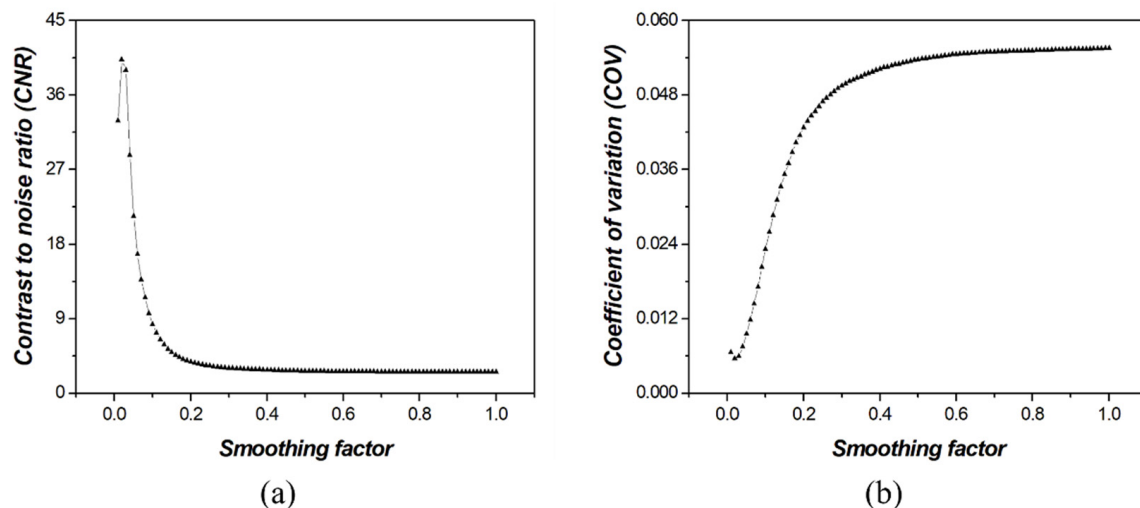

(a)   (b)

Figure 3. Quantitative evaluation results according to the smoothing factor of the fast non-local means algorithm in a virtual monoenergetic image: (**a**) contrast to noise ratio and (**b**) coefficient of variation.

3.2. The Comparative Evaluation of the Optimized Fast Non-Local Means Noise Reduction Algorithm with Conventional Algorithms

A comparative evaluation was conducted using SECT, DECT, and TV algorithms to evaluate the usefulness of the optimized FNLM. For comparison, the average CNR and COV values were measured at contrast agent concentrations of 20, 40, 60, 80, and 100%. Figure 4 shows the CNR and COV values for the optimized FNLM noise reduction, SECT, DECT, and TV algorithms. The CNR evaluation results show that the optimized FNLM noise reduction algorithm had the highest value of 40.2996, while the TV algorithm, DECT, and SECT had improvements of approximately 17.9663, 12.8084, and 9.3019, respectively. Additionally, the COV evaluation results show that the FNLM algorithm had the lowest COV value of 0.0055, while the TV algorithm, SECT, and DECT had values of approximately 0.0097, 0.0105, and 0.0135, respectively.
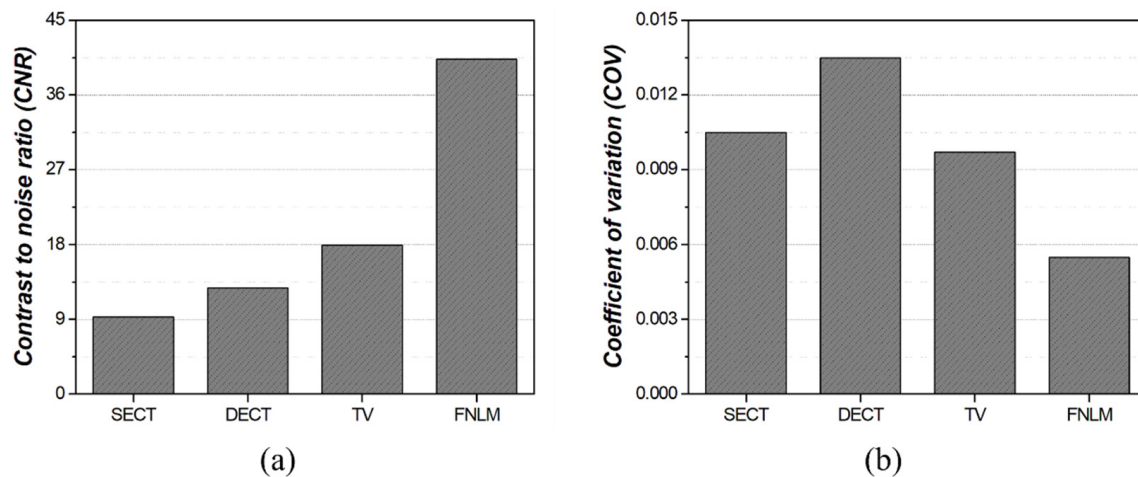
Figure 4. Comparative evaluation results of single-energy computed tomography, dual-energy computed tomography, the total variation noise reduction algorithm, and the optimized fast non-local means: (**a**) contrast to noise ratio and (**b**) coefficient of variation.

Moreover, we evaluated the NNPS of SECT, DECT, TV and optimized FNLM algorithms. Figure 5 shows the NNPS results. The results showed that the FNLM algorithm showed the greatest improvement, while DECT performed the least effectively. In particular, the optimized FNLM algorithm showed an average improvement of 10^{-1} mm^2 in the NNPS compared with the DECT image.
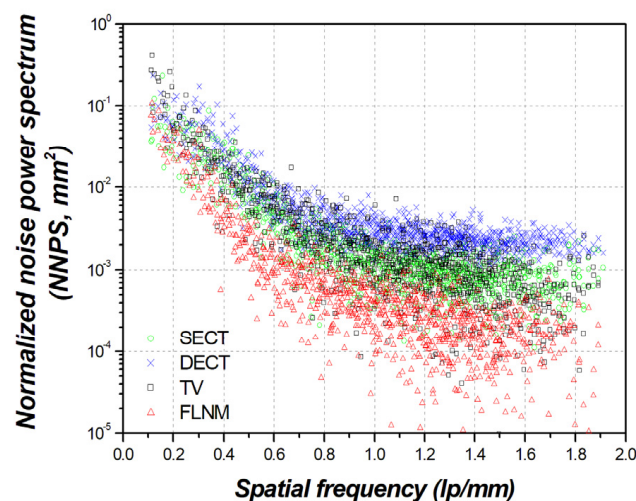

Figure 5. Comparative evaluation result of normalized noise power spectrum evaluation with single-energy computed tomography, dual-energy computed tomography, the total variation noise reduction algorithm, and the optimized fast non-local means.

3.3. The Visual Evaluation of the Optimized Fast Non-Local Means Noise Reduction Algorithm with Conventional Algorithms

A visual evaluation was performed to compare SECT, DECT, TV, and the optimized FNLM algorithm. Figure 6 shows the magnified region of the blue box in Figure 2 in the resulting image. The selected region contained a 100% contrast agent concentration sample, and the phantom was used to analyze the contrast of the contrast agent sample. The visual evaluation showed that the SECT image had a lower noise value than the DECT image, low contrast between the contrast sample and the phantom, and unclear sample edges. The DECT image showed a higher contrast between the contrast sample and the phantom than the SECT image; however, more noise was observed. The TV algorithm increased the overall brightness in both the phantom and contrast regions. Moreover, the

TV algorithm exhibited a relatively low noise reduction performance compared with the optimized FNLM algorithm. Additionally, the TV algorithm resulted in less smooth edges between the contrast sample and the phantom. The optimized FNLM algorithm effectively reduced noise without brightness distortion and produced the smoothest edges between the phantom and the contrast agent samples.
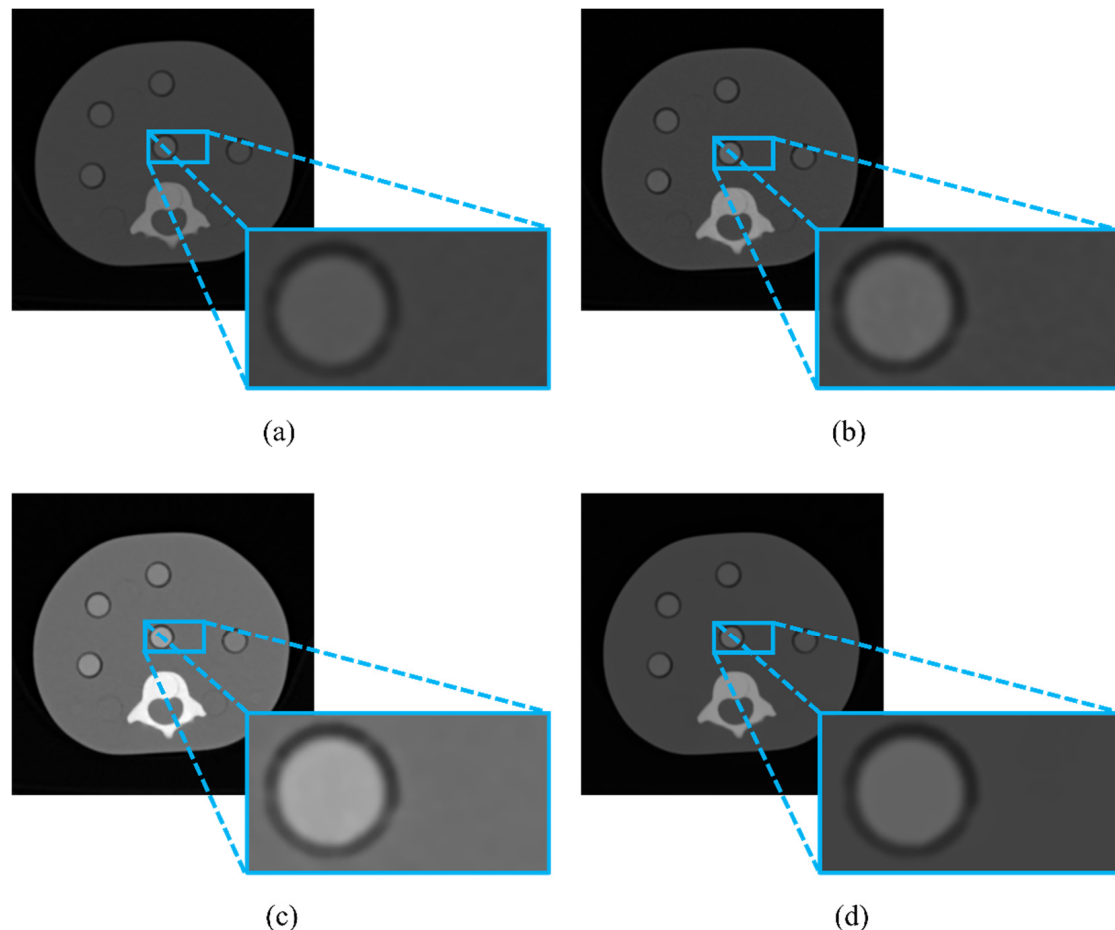

(a)

(b)

(c)

(d)

Figure 6. A magnified image of a contrast agent sample at 100% concentration for comparative visual evaluation: (**a**) single-energy computed tomography image, (**b**) dual-energy computed tomography image, (**c**) the total variation noise reduction algorithm, and (**d**) the optimized fast non-local means noise reduction algorithm.

4. Discussion

Abdominal CT is essential for patients with liver cancer; however, ultrasound and MRI are recommended for pediatric patients with liver cancer because of the risk of radiation exposure [30]. Abdominal CT scan is essential for pediatric patients with liver cancer undergoing liver transplantation, and contrast agents should be used to enhance liver vessel visualization [31]. However, contrast agents can cause nephrotoxicity, increasing the risk of side effects in pediatric patients who require repeated follow-up examinations [32]. To address this problem, a DECT-based VMI technique was proposed [33]. The VMI technique creates a virtual low-energy image with a low- and high-energy range acquired by DECT, providing high contrast with a low contrast agent dose [34]. However, DECT-based VMI can cause noise in images because of image acquisition in the low energy range, which can reduce the diagnostic accuracy in pediatric hepatic vascular imaging. In this study, the FNLM algorithm was applied and optimized to solve these noise problems, and its usefulness was confirmed by comparative evaluation with SECT, DECT-based VMI, and TV algorithms.

To optimize the FNLM algorithm, we measured the CNR and COV at various contrast concentrations (20, 40, 60, 80, and 100%). Both factors showed the most significant improvement at a smoothing factor of 0.02, and the rate of improvement slowed down after that. Based on these results, we derived an optimal smoothing factor of 0.02 for the FNLM algorithm on VMI. To confirm the usefulness of the optimal FNLM algorithm, we performed a comparative evaluation with SECT, DECT-based VMI, and TV algorithms. In the CNR and COV evaluation, the optimized FNLM algorithm performed the best, significantly improving CNR and COV by approximately 3.14 and 2.45 times, respectively, compared with DECT images. Additionally, the NNPS evaluation showed that the VMI image with the optimized FNLM algorithm was the most improved, with a 10^{-1} mm^2 improvement compared with the DECT image.

Visual evaluation confirmed that DECT images exhibited a higher contrast difference between the contrast agent sample and phantom compared with SECT images and that SECT images had lower contrast and less noise than DECT images. When comparing the TV algorithm with the optimized FNLM algorithm, we found that the TV algorithm retained noise, and an overall brightness increase was observed. The image obtained using the optimized FNLM algorithm effectively reduced the noise without distorting the signal, and the edges of the contrast agent samples were clearer. This indicates that the TV algorithm reduces noise by minimizing total variation ("sudden changes in the image"), leading to an overall smoothing effect by diminishing fine texture and gradient information [35]. The FNLM algorithm preserves detailed structures and edges more effectively because this approach uses a nonlinear filtering technique to reduce noise based on the similarity of the surrounding pixels. Because the FNLM algorithm selectively averages only similar patches, sharper edges are maintained compared with the TV algorithm, which can result in blurred boundaries [36]. Therefore, compared with the TV algorithm, the FNLM algorithm demonstrated superior performance in terms of noise reduction and structure preservation. These characteristics suggest that the FNLM algorithm can be widely applied in various fields owing to its flexibility and ability to adjust the parameters.

Several previous studies have shown that a 40 keV VMI provides the highest CNR because of the K-edge characteristics of the iodine contrast agent [37]. Another study confirmed that VMI images at 40 keV showed the highest attenuation; however, these images were noisier than images at other energy ranges [38]. In this study, the application of the FNLM algorithm effectively reduced the noise in a 40 keV VMI, allowing high-quality images to be acquired with a lower contrast dose. This reduction in the contrast dose is especially beneficial for pediatric patients because it minimizes the risk of contrast-induced toxicity.

Recent advances in deep learning have had a significant impact on medical imaging, particularly abdominal imaging [39]. One study demonstrated that a deep learning model can be effectively applied to pediatric patients with chronic liver disease with appropriate training [40]. However, training these models requires large datasets; in particular, deep learning-based denoising of CT images requires obtaining low-dose and standard-dose CT image sets from the same patient [41]. However, obtaining such large datasets of pediatric abdominal CT images is complex, and obtaining sufficient datasets for training is challenging because repeated scans are limited to pediatric patients owing to the risk of radiation exposure. To address this lack of datasets, FNLM algorithms are expected to be more applicable in clinical settings because they can effectively denoise only a single image and are computationally efficient.

Careful management of the radiation dose is essential in repeat abdominal CT scans of pediatric patients with liver cancer. When using DECT, the radiation dose is reduced by approximately 37% compared with SECT and can be reduced by approximately 47% depending on the protocol. This reduces radiation exposure and improves the life expectancy of pediatric patients [42]. Furthermore, DECT is more specialized than SECT for observing incidental lesions in other tissues, such as the spleen and kidneys, and DECT-acquired iodine maps can be generated to enhance the visualization of tumor nodules [43]. Addition-

ally, compared with MRI data, DECT can provide information on tissue composition, such as blood, iodine, calcification, and fat, and is particularly appropriate for iodine-specific imaging [44]. These advantages of DECT minimize radiation exposure in patients by avoiding unnecessary additional imaging or follow-up examinations. In one study, when DECT was used to image the abdomen of pediatric patients over eight years of age and the concentration of iodinated contrast was reduced, the image quality was not significantly different from that of SECT. This suggests that for pediatric abdominal diseases, DECT can be used to obtain diagnostically meaningful images with reduced doses of iodinated contrast [45].

Therefore, DECT-based liver cancer screening has been shown to significantly reduce effective contrast agent doses, which is particularly beneficial for pediatric patients who require repeated examinations. Furthermore, the results of this study can be applied to CT imaging of pediatric liver cancer patients, as well as in patients with various abdominal diseases.

Recent research has been conducted on multimodal medical fusion imaging systems. This approach extracts complementary and useful features from data from different modalities. In one study, an NLM-based algorithm was integrated into a fusion imaging system to reduce noise and improve sharpness in images, resulting in higher quality fused images [46]. Based on these findings, we plan to apply NLM-based algorithms in a multimodal framework to reduce noise in multimodality images and evaluate the impact of NLM-based algorithms. These studies are expected to serve as preliminary research to demonstrate how the properties of NLM-based algorithms in fusion imaging systems change important image qualities, such as contrast, sharpness, and information preservation. By analyzing the improvements that NLM-based algorithms contribute to medical image quality, we believe that we can provide the basis for a robust clinical imaging solution. Furthermore, we expect our future studies to demonstrate that NLM-based algorithms can improve individual image quality as well as overall medical modality imaging quality.

In conclusion, effective noise reduction with minimal radiation and contrast doses is essential for pediatric abdominal CT. This approach ensures diagnostic accuracy while reducing radiation exposure and contrast-induced toxicity. Many studies have focused on improving the quality of DECT-based images; however, most have been conducted in adult patients, and relatively few have addressed noise reduction in pediatric VMIs. This study is significant because it confirms the utility and applicability of noise reduction algorithms in pediatric VMIs and provides a framework for further research.

5. Conclusions

Minimizing radiation exposure and contrast agent doses is critical in pediatric abdominal CT scans, especially in pediatric patients with liver cancer who require repeat CT scans. Our study showed that the FNLM algorithm can significantly improve noise reduction at lower radiation and contrast agent doses without degrading image quality. This approach is beneficial for pediatric patients who require minimal exposure to radiation and contrast agent toxicity. Previous research has focused on improving image quality with DECT in adult patients; however, relatively few studies have addressed noise reduction in pediatric VMI imaging. This study demonstrates that the FNLM algorithm can effectively reduce noise while maintaining diagnostic quality, providing a solution for pediatric patients with liver cancer and other pediatric abdominal imaging needs. These results provide a framework for further research on the application of advanced noise reduction algorithms in pediatric imaging, potentially contributing to safer and more efficient diagnostic practices in clinical settings.

Data Availability Statement: The raw data supporting the conclusions of this article will be made available by the authors on request.

Conflicts of Interest: The authors declare no conflicts of interest.

References

1. Martin, C.J. Optimisation in general radiography. *Biomed. Imaging Interv. J.* **2007**, *3*, e18. [CrossRef] [PubMed]
2. Organization for Economic Co-operation and Development (OECD). Computed Tomography (CT) Exam. 2021. Available online: https://data.oecd.org/healthcare/computed-tomography-ct-exams.htm (accessed on 29 November 2023).
3. Chodick, G.; Kim, K.P.; Shwarz, M.; Horev, G.; Shalev, V.; Ron, E. Radiation risks from pediatric computed tomography scanning. *Pediatr. Endocrinol. Rev.* **2009**, *7*, 29–36. [PubMed]
4. Dupuy, D.; Costello, P.; Lewis, D.; Jenkins, R. Abdominal CT findings after liver transplantation in 66 patients. *AJR Am. J. Roentgenol.* **1991**, *156*, 1167–1170. [CrossRef] [PubMed]
5. Al Mahrooqi, K.M.S.; Ng, C.K.C.; Sun, Z. Pediatric computed tomography dose optimization strategies: A literature review. *J. Med. Imaging Radiat. Sci.* **2015**, *46*, 241–249. [CrossRef] [PubMed]
6. Dong, F.; Davros, W.; Pozzuto, J.; Reid, J. Optimization of kilovoltage and tube current–exposure time product based on abdominal circumference: An oval phantom study for pediatric abdominal CT. *AJR Am. J. Roentgenol.* **2012**, *199*, 670–676. [CrossRef]
7. Andreucci, M.; Faga, T.; De Sarro, G.; Michael, A. The toxicity of iodinated radiographic contrast agents in the clinical practice. *J. Nephrol. Adv.* **2015**, *1*, 6–41. [CrossRef]
8. Thomson, K.R.; Varma, D.K. Safe use of radiographic contrast media. *Aust. Prescr.* **2010**, *33*, 19–22. [CrossRef]
9. Kreisler, B. Photon counting Detectors: Concept, technical Challenges, and clinical outlook. *Eur. J. Rad.* **2022**, *149*, 110229. [CrossRef]
10. Rajendran, K.; Voss, B.A.; Zhou, W.; Tao, S.; DeLone, D.R.; Lane, J.I.; Weaver, J.M.; Carlson, M.L.; Fletcher, J.G.; McCollough, C.H.; et al. Dose reduction for sinus and temporal bone imaging using photon-counting detector CT with an additional tin filter. *Invest. Rad.* **2020**, *55*, 91–100. [CrossRef]
11. Jungblut, L.; Blüthgen, C.; Polacin, M.; Messerli, M.; Schmidt, B.; Euler, A.; Alkadhi, H.; Frauenfelder, T.; Martini, K. First performance evaluation of an artificial intelligence-based computer-aided detection system for pulmonary nodule evaluation in dual-source photon-counting detector CT at different low-dose levels. *Invest. Rad.* **2022**, *57*, 108–114. [CrossRef]
12. Aran, S.; Shaqdan, K.W.; Abujudeh, H.H. Dual-energy computed tomography (DECT) in emergency radiology: Basic principles, techniques, and limitations. *Emerg. Radiol.* **2014**, *21*, 391–405. [CrossRef] [PubMed]
13. Riederer, S.J.; Mistretta, C.A. Selective iodine imaging using K-edge energies in computerized x-ray tomography. *Med. Phys.* **1977**, *4*, 474–481. [CrossRef] [PubMed]
14. Sato, E.; Oda, Y.; Abudurexiti, A.; Hagiwara, O.; Matsukiyo, H.; Osawa, A.; Enomoto, T.; Watanabe, M.; Kusachi, S.; Sato, S.; et al. Demonstration of enhanced iodine K-edge imaging using an energy-dispersive X-ray computed tomography system with a 25 mm/s-scan linear cadmium telluride detector and a single comparator. *Appl. Radiat. Isot.* **2012**, *70*, 831–836. [CrossRef] [PubMed]
15. Shim, J.; Kim, K.; Lee, Y. Effect of iodine concentration reduction by comparison of virtual monoenergetic image quality with dual-energy computed tomography. *Appl. Radiat. Isot.* **2023**, *200*, 110967. [CrossRef] [PubMed]
16. Sugrue, G.; Walsh, J.P.; Zhang, Y.; Niu, B.; Macri, F.; Khasanova, E.; Metwally, O.; Murray, N.; Nicolaou, S. Virtual monochromatic reconstructions of dual energy CT in abdominal trauma: Optimization of energy level improves pancreas laceration conspicuity and diagnostic confidence. *Emerg. Radiol.* **2021**, *28*, 1–7. [CrossRef]
17. Wichmann, J.L.; Gillott, M.R.; De Cecco, C.N.; Mangold, S.; Varga-Szemes, A.; Yamada, R.; Otani, K.; Canstein, C.; Fuller, S.R.; Vogl, T.J.; et al. Dual-energy computed tomography angiography of the lower extremity runoff: Impact of noise-optimized virtual monochromatic imaging on image quality and diagnostic accuracy. *Invest. Radiol.* **2016**, *51*, 139–146. [CrossRef]
18. Zeng, Y.; Geng, D.; Zhang, J. Noise-optimized virtual monoenergetic imaging technology of the third-generation dual-source computed tomography and its clinical applications. *Imaging Med. Surg.* **2021**, *11*, 4627–4643. [CrossRef]
19. Hanson, G.J.; Michalak, G.J.; Childs, R.; McCollough, B.; Kurup, A.N.; Hough, D.M.; Frye, J.M.; Fidler, J.L.; Venkatesh, S.K.; Leng, S.; et al. Low kV versus dual-energy virtual monoenergetic CT imaging for proven liver lesions: What are the advantages and trade-offs in conspicuity and image quality? A pilot study. *Abdom. Radiol.* **2018**, *43*, 1404–1412. [CrossRef]
20. Deng, G.; Cahill, L.W. An adaptive Gaussian filter for noise reduction and edge detection. In Proceedings of the IEEE Conference Record Nuclear Science Symposium and Medical Imaging Conference, San Francisco, CA, USA, 30 October–6 November 1993; Volume 1993, pp. 1615–1619. [CrossRef]
21. Hoeher, P.; Kaiser, S.; Robertson, P. Two-dimensional pilot-symbol-aided channel estimation by Wiener filtering. In Proceedings of the 1997 IEEE International Conference on Acoustics [Speech], Munich, Germany, 21–24 April 1997; Volume 3, pp. 1845–1848. [CrossRef]
22. Buades, A.; Coll, B.; Morel, J.M. A non-local algorithm for image denoising. In Proceedings of the IEEE Computer Society Conference on Computer Vision and Pattern Recognition (CVPR'05), San Diego, CA, USA, 20–26 June 2005; Volume 2, pp. 60–65. [CrossRef]

23. Darbon, J.; Cunha, A.; Chan, T.F.; Osher, S.; Jensen, G.J. Fast nonlocal filtering applied to electron cryomicroscopy. In Proceedings of the 5th IEEE International Symposium on Biomedical Imaging: From Nano to Macro, Paris, France, 14–17 May 2008; Vol 2008; pp. 1331–1334. [CrossRef]

24. Dauwe, A.; Goossens, B.; Luong, H.Q.; Philips, W. A fast non-local image denoising algorithm. *Image Process Algor. Syst.* **2008**, *6812*, 324–331. [CrossRef]

25. Buades, A.; Coll, B.; Morel, J.M. A review of image denoising algorithms, with a new one. *Multiscale Model. Simul.* **2005**, *4*, 490–530. [CrossRef]

26. Yan, J.; Schaefferkoetter, J.; Conti, M.; Townsend, D. A method to assess image quality for low-dose PET: Analysis of SNR, CNR, bias and image noise. *Cancer Imaging* **2016**, *16*, 36. [CrossRef] [PubMed]

27. Doughty, M.J.; Aakre, B.M. Further analysis of assessments of the coefficient of variation of corneal endothelial cell areas from specular microscopic images. *Clin. Exp. Optom.* **2008**, *91*, 438–446. [CrossRef] [PubMed]

28. Rudin, L.I.; Osher, S.; Fatemi, E. Nonlinear total variation based noise removal algorithms. *Phys. D Nonlinear Phenom.* **1992**, *60*, 259–268. [CrossRef]

29. Martin, R. Noise power spectral density estimation based on optimal smoothing and minimum statistics. *IEEE Trans. Speech Audio Process.* **2001**, *9*, 504–512. [CrossRef]

30. Jo, Y.; Kim, J.; Park, C.H.; Lee, J.W.; Hur, J.H.; Yang, D.H.; Lee, B.Y.; Im, D.J.; Hong, S.J.; Kim, E.Y.; et al. Quantitative imaging in pediatric hepatobiliary disease. *Korean J. Radiol.* **2019**, *20*, 1342–1357. [CrossRef]

31. Cannella, R.; Zins, M.; Brancatelli, G. ESR Essentials: Diagnosis of hepatocellular carcinoma—Practice recommendations by ESGAR. *Eur. Radoil.* **2024**, *34*, 2127–2139. [CrossRef]

32. Kaller, M.O.; An, J. *Contrast Agent Toxicity*; StatPearls Publishing: Treasure Island, FL, USA, 2019.

33. D'Angelo, T.; Cicero, G.; Mazziotti, S.; Ascenti, G.; Albrecht, M.H.; Martin, S.S.; Othman, A.E.; Vogl, T.J.; Wichmann, J.L. Dual energy computed tomography virtual monoenergetic imaging: Technique and clinical applications. *Br. J. Radiol.* **2019**, *92*, 20180546. [CrossRef]

34. Li, G.; Rednam, N.; Kundra, V. Low KeV virtual monoenergetic images for detecting low dose iodine-or alternative Gd-based IV contrast agents. *Heliyon* **2024**, *10*, e35210. [CrossRef]

35. Tang, L.; Fang, Z. Edge and contrast preserving in total variation image denoising. *EURASIP J. Adv. Signal Process.* **2016**, *2016*, 13. [CrossRef]

36. Shim, J.; Yoon, M.; Lee, Y. Comparison of filtered back projection with fast non-local means denoising approach and iterative reconstruction in pediatric chest CT image using 3D printed lung nodules. *J. Korean Phys. Soc.* **2023**, *82*, 1114–1123. [CrossRef]

37. Al-Baldawi, Y.; Große Hokamp, N.G.; Haneder, S.; Steinhauser, S.; Püsken, M.; Persigehl, T.; Maintz, D.; Wybranski, C. Virtual mono-energetic images and iterative image reconstruction: Abdominal vessel imaging in the era of spectral detector CT. *Clin. Rad.* **2020**, *75*, 641.e9–641.e18. [CrossRef] [PubMed]

38. Große Hokamp, N.; Höink, A.J.; Doerner, J.; Jordan, D.W.; Pahn, G.; Persigehl, T.; Maintz, D.; Haneder, S. Assessment of arterially hyper-enhancing liver lesions using virtual monoenergetic images from spectral detector CT: Phantom and patient experience. *Abdom. Radiol. (NY)* **2018**, *43*, 2066–2074. [CrossRef] [PubMed]

39. Zhang, Z.; Sejdić, E. Radiological images and machine learning: Trends, perspectives, and prospects. *Comput. Biol. Med.* **2019**, *108*, 354–370. [CrossRef] [PubMed]

40. Azer, S.A. Deep learning with convolutional neural networks for identification of liver masses and hepatocellular carcinoma: A systematic review. *World J. Gastrointest. Oncol.* **2019**, *11*, 1218–1230. [CrossRef] [PubMed]

41. Lee, S.; Choi, Y.H.; Cho, Y.J.; Lee, S.B.; Cheon, J.E.; Kim, W.S.; Ahn, C.K.; Kim, J.H. Noise reduction approach in pediatric abdominal CT combining deep learning and dual-energy technique. *Eur. Radiol.* **2021**, *31*, 2218–2226. [CrossRef]

42. Lestra, T.; Mulé, S.; Millet, I.; Carsin-Vu, A.; Taourel, P.; Hoeffel, C. Applications of dual energy computed tomography in abdominal imaging. *Diagn. Interv. Imaging* **2016**, *97*, 593–603. [CrossRef]

43. Wortman, J.R.; Bunch, P.M.; Fulwadhva, U.P.; Bonci, G.A.; Sodickson, A.D. Dual-energy CT of incidental findings in the abdomen: Can we reduce the need for follow-up imaging? *AJR Am. J. Roentgenol.* **2016**, *207*, W58–W68. [CrossRef]

44. Smith, E.A.; Dillman, J.R. Current role of body MRI in pediatric oncology. *Pediatr. Radiol.* **2016**, *46*, 873–880. [CrossRef]

45. Kang, Y.; Hwang, S.H.; Han, K.; Shin, H.J. Comparison of image quality, contrast administration, and radiation doses in pediatric abdominal dual-layer detector dual-energy CT using propensity score matching analysis. *Eur. J. Radiol.* **2023**, *169*, 111177. [CrossRef]

46. Rajakumar, S.; Sreedhar, P.S.S.; Kamatchi, S.; Tamilmani, G. Gray wolf optimization and image enhancement with NLM Algorithm for multimodal medical fusion imaging system. *Biomed. Signal Process. Control.* **2023**, *85*, 104950. [CrossRef]